

Final Draft
of the original manuscript:

Wang, F.F.; Li, W.Y.; Shen, J.J.; Hu, S.Y.; Li, J.L.; dos Santos, J.F.; Huber, N.:
Effect of tool rotational speed on the microstructure and mechanical properties of bobbin tool friction stir welding of Al-Li alloy

In: Materials and Design (2015) Elsevier

DOI: 10.1016/j.matdes.2015.07.096

Effect of tool rotational speed on the microstructure and mechanical properties of bobbin tool friction stir welding of Al-Li alloy

F.F. Wang^{a, b, *}, W.Y. Li^{a,*}, J. Shen^b, S.Y. Hu^b, J.F. dos Santos^b

^a State Key Laboratory of Solidification Processing, Shaanxi Key Laboratory of Friction Welding Technologies, Northwestern Polytechnical University, Xi'an 710072, Shaanxi, PR China

^b Helmholtz-Zentrum Geesthacht, Institute of Materials Research, Materials Mechanics, Geesthacht 21502, Germany

Corresponding author: F.F. Wang, Tel.: +49-4152-872313, Fax: +49-4152-872033, Email: feifan.wang@hzg.de

W.Y. Li, Tel.: ++86-29-88495226, Fax: ++86-29-88491426, Email: liwy@nwpu.edu.cn

Abstract

A third-generation Al-Li alloy AA2198 has been successfully welded by bobbin tool friction stir welding. The stirred zone, displaying an hourglass shape, consists of recrystallized Al grains and precipitates remaining in solution. Joint line remnants have been found in all etched welds. Symmetrical hardness profiles have been obtained in the thickness direction, which indicates that the joints have homogenous through-thickness mechanical properties. As the rotational speed increases, the grain size of the stirred zone increases, whereas the density of strengthening particles decreases; the joint line remnants become compressed remarkably in the shoulder-dominated zone while less changes occur in the probe-dominated zone; the softest region shrinks and shifts outward, the average hardness of the stirred zone increases and the hardness profile along the cross section of the joint changes from the U-shaped to W-shaped. The tensile strength of the joint initially increases with rotational speed and then decreases with the maximal strength efficiency reaching 80%; three fracture modes have been observed and cracking initiates at the joint line remnant propagating towards the heat-affected zone, and finally to the border between the thermal-mechanically affected zone and stirred zone.

Keywords: Friction stir welding; bobbin tool; Al-Li alloy; microstructure; joint line remnant; mechanical properties

1. Introduction

Due to the high specific strength and stiffness combined with good damage tolerance properties, the third-generation Al-Li alloys have been developed for aircraft and spacecraft applications to improve the fuel efficiency and payload capability [1, 2]. However, joining Al-Li alloys by fusion welding processes is challenging due to the associated solidification defects such as hot cracking and porosity [2-4].

Bobbin tool friction stir welding (BT-FSW), is a variant of the friction stir welding (FSW) process and has potential advantages over fusion welding of Al-Li alloys [5]. Compared with the tool used in standard (single-sided) FSW, the bobbin tool has an extra shoulder attached to the tip of the probe, namely the lower shoulder. This setup makes BT-FSW capable of joining closed profiles like hollow extrusions [6,7]. Also, root flaws such as lack of penetration (LOP), sometimes reported in standard FSW, can be completely avoided. Additionally, more uniform through-thickness mechanical properties were reported for BT-FSW [8].

So far, investigations on the microstructure and joint mechanical properties developed in BT-FSW have focused primarily on 6000 series aluminum alloys [9-12]. There has been comparatively little work on the development of BT-FSW of high-strength Al alloys especially in the case of Al-Li alloys [8,13]. Skinner et al. [8] and Schneider et al. [13] pointed out that the tensile strength of AA2195 joint produced by BT-FSW met or exceeded that by standard FSW, but there was no detail on the microstructure involved in their work. In addition, rotational speed is a very important welding parameter, which plays a key role on the material flow and heat generation, thereby influencing the microstructures and mechanical properties of joint. Schneider et al. [13] found that the rotational speed has a significant effect on the shape of weld zone and

joint strength. However, the fracture location and mechanisms of welds were not studied, which would be of high interest in welding of the high strength Al-Li alloys.

Concerning studies on BT-FSW of Al-Li alloys, no systematic investigation has been carried out so far. Besides, no work has been reported on BT-FSW of the Al-Li alloy AA2198, which is the subject of the present investigation. The main purposes of this study are to investigate the application of BT-FSW on an alloy AA2198-T851 and determine the effect of rotational speed on the microstructure and mechanical properties of the obtained joints.

2. Material and experimental procedures

The base material (BM) used in the present work is an AA2198 alloy sheet with a dimension of 250 mm long by 100 mm wide, supplied as a 3.2 mm thickness in a T851 temper (solution heat treated, stress relieved by stretching, and finally artificially aged). The nominal composition is shown in Table 1. The plates were butt welded parallel to the rolling direction by a custom designed FSW machine (FlexiStir) using a controlled gap size of 3 mm. The welding tool is made of a nickel-cobalt alloy MP159 with two shoulders of 11 mm in diameter and a cylindrical featureless probe of 4 mm in diameter. The range of the tool rotational speeds investigated varied between 400 and 1000 rpm, as shown in Table 2, whereas the welding speed is fixed as 42 mm/min. Additionally, the resultant gap force, torque and heat index are also listed in Table 2. It is noted that the heat index (HI) value represents heat input per unit length, which is estimated through $HI = \frac{2\pi\omega\Gamma}{60v}$, where ω is the rotational speed, Γ is the tool torque and v is the welding speed.

All welded specimens were examined one month after welding, by which time any natural aging would have stabilized. Samples for microstructure analysis were cut perpendicular to the welding direction, mechanically ground and polished, etched using the Keller's Reagent (2 ml

HF, 3 ml HCl, 5 ml HNO₃, and 190 ml H₂O), and examined by optical microscopy (OM). A suitable surface finish for electron backscatter diffraction (EBSD) was achieved by applying mechanical polishing in a similar fashion followed by vibration polishing. The hardness measurements were conducted applying a 0.2 kg load for 10 s on a Vickers hardness tester. Using the same settings 2D hardness maps of the cross sections were also obtained using an UTS100 hardness tester. Tensile samples were cut perpendicular to the weld direction into a dog-bone shape with a gauge of 70 mm long by 12.5 mm wide according to ASTM E8/E8M-13a [14], and tensile tests were performed in triplicate for each welding parameter at a head cross speed of 1 mm/min by using a testing machine. Fracture surfaces of tensile samples and BM were observed using a scanning electron microscope (SEM).

3. Results and discussion

3.1. Thermal cycles

During welding the workpieces experienced a rapid heating and cooling as well as a massive plastic deformation characteristic of the FSW process, resulting in a complex microstructure formation. Strengthening phases dissolve and/or re-precipitated within the weld zone [15]. Fig. 1 shows the effect of different rotational speeds on the recorded welding thermal cycles. The thermocouples were placed at the mid-plane of the plate on the advancing side (AS), 10 mm away from the weld center. It can be seen that the peak temperature increases from 252 to 330°C with the rotational speed increasing from 400 rpm to 1000 rpm. Moreover, the elevated-temperature (typically over 150°C) exposure time t_{150} increases from 57 to 100 s as the rotational speed increases from 400 rpm to 1000 rpm. These facts indicate that a higher rotational speed produces more heat input, which also agrees well with the estimated heat index as shown in Table 2.

Although the weld heat input in per unit length of weld can be calculated using the torque based weld power model, the heat generation mechanism of BT-FSW is very complex and depends on the friction and the plastic deformation works occurred in the weld zone. Obviously, it is also closely related to the properties of BM at high temperature, friction coefficient, corresponding material flow and etc. In this study, it can be found that an increasing rotational speed leads to a higher heat input, making a lower material flow stress, torque and gap force between the rotating tool and the workpieces.

3.2. Microstructure characteristics

Fig. 2a shows the cross-section macrograph of a typical joint produced with 600 rpm (see Table 2). Unlike in conventional FSW, the SZ in the BT-FSW has a compressed hourglass shape. That is, the two weld extremities possess the largest diameter (slightly larger than that of the shoulders) while the weld mid-plane displays the smallest diameter (larger than that of the probe). The reason for this shape is related to the special material flow conditions imposed by the upper and lower shoulders [16]. On the other hand, similar to standard FSW, the joint also exhibits four different microstructural zones, i.e. SZ, thermo-mechanically affected zone (TMAZ), heat-affected zone (HAZ), and BM. Details on the observed grain morphology of the different zones are shown in Table 3. It should be mentioned that the grain size as measured by the EBSD technique and by optical microscopy are comparable, and therefore the grain size hereinafter will be referred to as the one measured by the optical microscopy, if not referred otherwise. Compared with the BM having highly elongated grains (Fig. 2b), the SZ (Fig. 2d) has much smaller equiaxed recrystallized grains; the TMAZ (Figs. 2c and 2e) has mixed rotated elongated grains and equiaxed grains, i.e. grains of partially recrystallized morphology; the HAZ, however, has almost no detectable change (image not shown) by either the optical microscopy or the

EBSD technique (see Table 3). In addition, a sharp transition can be seen between the TMAZ and the SZ on the AS while a much more diffuse interface at the RS is observed, which is related to different material flow conditions on the two sides.

The SZ microstructures formed at different rotational speeds are shown in Figs. 3a-d. It can be seen that the average size of recrystallized grains increases from 2.1 μm to 6.0 μm with increasing rotational speeds from 400 rpm to 1000 rpm. Moreover, for a low rotational speed, e.g., 400 rpm, some particles Al₇Cu₂Fe (indicated by the white arrow in Fig. 3a, identified by the integrated EBSD and energy dispersive spectroscopy technique; result not shown in the present work) pre-existing in the BM can be found in the resultant SZ. This phase prevails in Al-Li alloys as an insoluble particle and is hardly affected by heat treatments [2]. For increasing rotational speeds, no particles in solution could be observed (see Figs. 3b-d). Since these particles are insoluble, exposure at elevated temperatures should hardly influence their precipitation-dissolution behavior. One possible explanation for this phenomenon is that the mechanical milling effect, characteristic of the welding process, caused the breakup of the Al₇Cu₂Fe particles. This effect is probably not so prominent at lower rotational speeds, leaving some pre-existing particles unaffected. In this sense, a rotational speed higher than 400 rpm is necessary since this insoluble particles compromise the mechanical properties of the joint [2].

3.3. Joint line remnant and material flow

Joint line remnant (JLR) is often observed in the FSW and interpreted as remnant oxide films originated from the butt interface during welding [17-22]. Generally, the JLR does not cause loss of mechanical properties of as-welded joints [18, 20, 22], but it seriously compromises those of heat-treated joints [20] and also results in preferential etching [18]. It is thus undesirable, especially for heat-treatable Al alloys. Interestingly, it is noted that JLRs are difficult to be

revealed by a micro etchant such as Keller's Reagent (see Fig. 2a) while they can be clearly revealed by a macro etchant such as 2% NaOH (Fig. 4a).

The JLRs are visible in all welds, as shown in Fig. 4a. From a magnified SEM image, as shown in Fig. 4b, it can be seen that the JLR is actually a band rather than a line. In this region, a large number of pits can be seen and most of them are located at grain boundaries. These pits are probably resulted from the sample preparation, which makes hard particles (oxides) peel off from the aluminum matrix. This hypothesis is consistent with the conclusion of a study based on focused ion beam-assisted transmission electron microscopy [18]. Moreover, as shown in Fig. 4a, with increasing the rotational speed from 400 rpm to 1000 rpm, the JLR becomes gradually compressed, i.e. the length of the JLR becomes shorter in both the horizontal and vertical directions. This fact can probably be attributed to a higher degree of stirring caused by higher rotational speed leading to the wider and more dilute distribution of the oxide particles [19, 21].

In our previous work [16], the SZ was divided into different zones depending on the role of the shoulder and probe in the local material flow: the two zones in direct contact with the shoulders are referred to as the shoulder-dominated zone (SDZ) and the rest are the probe-significant and shoulder-partial dominated zone (PSZ). A schematic diagram of the overlaid JLR on the BT-FSW joints is illustrated in Fig. 4c. In some sense, the JLR reflects the local material flow within the SZ. When the rotational speed is low, e.g. 400 rpm, the JLR almost exists through the thickness; when the rotational speed is higher, it is confined within a smaller range, corresponding to the PSZ. This indicates the increase in rotational speed can evidently increase the local material flow in the SDZ for this thin sheet material. However, the rotational speed has less influence on the local material flow in the PSZ, because the cylindrical probe is of a small

diameter and featureless. Therefore, the JLRs are obvious in the PSZ of all joints produced with different rotational speeds, which may affect the joint strength and fracture behavior.

3.4. Mechanical properties

3.4.1 Microhardness

Fig. 5a shows the mid-thickness hardness profiles of welds at different rotational speeds. Two typical characteristic hardness profiles, i.e. the U-shaped and the W-shaped, are observed along the cross section and schematically shown in Fig. 5b. For low rotational speed, e.g. 400 rpm, the hardness drops progressively before reaching a minimum of 85 Hv (59% of the BM) near the edge of the SZ, and rises slightly to a level of 88 Hv within the center SZ. That is, a U-shaped hardness profile is obtained along the cross section. With increasing rotational speeds, e.g. 600-1000 rpm, the hardness rises above 104 Hv within the SZ after reaching a minimum; this indicates that W-shaped hardness profiles are obtained.

It is well known that the hardness softening throughout weld zone is principally related to the coarsening and dissolution of strengthening precipitates during welding imposed by the thermal cycle and plastic deformation in Al-Cu-Li alloys [22]. The hardness of the SZ can also be significantly influenced by further precipitation during and after cooling dependent on the peak temperature and duration of the thermal cycle. This is manifested by the differences in characteristic hardness profiles. The typical W-shaped hardness profile with some hardness recovery could be mainly due to the post-weld natural ageing (PWNA) response in the SZ. This has been widely reported in high-strength aluminium alloy welds, where hardness recovers over time with a further precipitation occurs during PWNA, in cases of supersaturated solute remaining in the weld after a fast cooling down from a substantial solution [23-26]. Therefore, it can be inferred that, as the rotational speed increases from 400 to 1000 rpm, the peak

temperature and the exposure time increases, the degree of supersaturation remaining increases, the PWNA response is greater, and the hardness recovery in center SZ is more obvious (W-shaped profile).

Fig. 5c shows the hardness maps (superimposed with the TMAZ borders) of joints in the cross section. It can be found that all samples show a roughly symmetrical hardness distribution in the thickness direction, due to the symmetrical heat generation and material flow induced by upper and lower shoulders. Moreover, with increasing the rotational speed, the softest region (enclosed by pink lines) decreases in area and is shifted outward. This effect reflects the intercept length of a critical temperature on the temperature distribution curve (temperature vs. distance), which increases with the rotational speed. As we known, in FSW of heat-treatable Al alloys, the softest region (minimum hardness) reported is either located in the HAZ [21, 27] or in the TMAZ [28]. The softest region is always related to the fracture location and morphology of the joint under loading. Therefore, the hardness map could be beneficial for explaining the resultant joint strength and fracture morphology.

3.4.2. Tensile strength

Fig. 6 presents the tensile results of joints produced at different rotational speeds as well as that of the BM. It should be noted that no polishing has been done on the weld surface, and tensile strength of specimen were calculated using the nominal BM thickness of 3.2mm. It can be found that the ultimate tensile strength (UTS), yield strength (YS), and elongation to fracture of bobbin tool friction stir welds of AA2198 are inferior to those of the BM. The UTS of the joint first increases as the rotational speed increases, reaching a maximum strength of 379 MPa at the 800 rpm, then decreases as the rotational speed further increases to 1000 rpm. The maximal UTS is 80% of that of the BM. Thus the joint has a comparable strength to that reported for standard

FSW of AA2198 alloy (joint efficiency of 78%-80% [29] and 59%-71% [30]). Moreover, the yield strengths of all welds are almost the same at around 250 MPa, which is only half of that of the BM. Thus, the work hardening capacity of the sound welds is substantially higher than that of the BM. Additionally, the BT-FSW joint is a heterogeneous composite and its different component parts, including their interfaces, possess different mechanical properties. The weakest region in the joint is more susceptible to the stress and strain concentration under tensile loading. That is the reason why the global elongations of the BT-FSW joints are much lower than that of the BM.

3.4.3. Fracture location and morphology

Fig. 7 shows the fracture locations of joints produced at different rotational speeds. Three fracture modes can be recognized, defined as Mode I, Mode II, and Mode III. In Mode I, failure occurs in the SZ, as shown in Figs. 7a-7c, 7e. In Mode II, failure occurs at the HAZ (see also Fig. 5b), as shown in Fig. 7d. In Mode III, failure occurs at the border of the TMAZ/SZ, as shown in Fig. 7f. Among them, Mode I is the most common one regardless of the welding conditions. In this mode, considering the respective hardness maps (see Fig. 5b) the crack initiation sites do not correlate to any softened regions within the SZ. However, if the respective weld macrographs (see Fig. 4a) are considered, the initiation sites coincide well with the JLR. Therefore, more specifically, in Mode I, failure occurs right at the JLRs. In these joints, the JLRs play a key role on the joint fracture behavior. This, however, is not commonly seen in standard FSW. It also should be noted that when the rotational speed is relatively low, e.g. 400-600 rpm (see Figs. 7a-7b), Mode I is the observed fracture mode. When the rotational speed is higher, e.g. 800 rpm, a larger degree of stirring is created and this makes the JLR region more scattered or stronger; and if this is the case, the softest region, i.e. the HAZ (see Fig. 5b), could be more favorable for the

crack initiation, that is, the Mode II. When the rotational speed further increases, e.g. 1000 rpm, the area of the softest region is very limited (see Fig. 5b), minor discontinuities, such as the border of the TMAZ/SZ, also possibly favor for the crack initiation, and then Mode III occurs.

Fig. 8 shows typical fracture morphologies corresponding to Modes I-III, i.e. the positions (a) to (c) in Fig. 7, as well as that from the BM. Although the fracture behavior is related to the JLR in Mode I, no remnant (oxide) particles could be observed on the fracture surface (Fig. 8a). Nevertheless, the dimples are smaller than that on the BM fracture surface (Fig. 8d). For Mode II, the initial rolling direction of the plate is still seen in the fracture surface (Fig. 8b) since the fracture occurred in the HAZ. While for Mode III, it is similar to those fractures occurring at weld discontinuities or weak metallic bonds, which are frequently found on the AS between TMAZ and SZ at non-optimal material flow conditions [6,10,11].

4. Conclusions

In this paper, AA2198-T851 alloy was successfully welded by BT-FSW using different rotational speeds. The typical microstructure and mechanical properties of joints are investigated. The effects of rotational speed on the microstructure and tensile properties are also discussed. The following conclusions could be drawn:

- (1) BT-FSW creates an hourglass-shape SZ. The resulting joint is composed of the recrystallized SZ, the partially recrystallized TMAZ, the little affected HAZ and the unaffected BM. As rotational speed increases, the grain size of the SZ increases and the insoluble phase $\text{Al}_7\text{Cu}_2\text{Fe}$ is broken up from the stirring action of the BF-FSW tool.
- (2) JLR exists in all etched welds. As rotational speed increases, the JLR is compressed remarkably in the SDZ while a less change occurs in PSZ with a tendency to shift towards the RS.

- (3) Symmetrical hardness distributions are obtained in the thickness direction for all welds, indicating through-thickness homogeneity of mechanical properties in the BT-FSW. As rotational speed increases, the softest region shrinks and shifts outward, the average hardness of the SZ increases and the hardness distribution along the cross section of joint changes from the U-shaped to W-shaped.
- (4) As rotational speed increases, the joint tensile strength increases first and then decreases. The maximal strength efficiency is 80%. Three typical fracture modes are found depending on the cracking initiation site. As the rotational speed increases, the most frequent fracture mode changes, i.e. failure initiates from the JLR to the HAZ continuing to the TMAZ/SZ border.

Acknowledgment

Feifan Wang would like to acknowledge the China Scholarship Council (No.201306290117) for the financial support. This work has been carried out under the auspices of the Cooperation Agreement between the School of Material Sciences and Engineering of the Northwest Polytechnical University and the Helmholtz-Zentrum Geesthacht (HZG 161/2014 and 111 Project / B08040).

References

- [1] R.J. Rioja, J. Liu, The evolution of Al-Li base products for aerospace and space applications, Metall. Mater. Trans. A 43 (2012) 3325-3337.
- [2] N.E. Prasad, A.A. Gokhale, R.J.H. Wanhill, editors. Aluminum-lithium alloys. Boston: Butterworth-Heinemann, 2014.
- [3] T. Dursuna, C. Soutis, Recent developments in advanced aircraft aluminium alloys, Mater. Des. 56 (2014) 862-871.
- [4] R. Xiao, X. Zhang, Problems and issues in laser beam welding of aluminum-lithium alloys, J. Manuf. Process. 16 (2013) 166-175.

- [5] G. Çam and S. Mistikoglu, Recent developments in friction stir welding of Al-alloys, *J. Mater. Eng. Perform.* 23 (2014)1936-1953.
- [6] W.Y. Li, T. Fu, L. Hütsch, J. Hilgert, F.F. Wang, J.F. dos Santos, N. Huber, Effects of tool rotational and welding speed on microstructure and mechanical properties of bobbin-tool friction-stir welded Mg AZ31, *Mater. Des.* 64 (2014) 714-720.
- [7] Y.X. Huang, L. Wan, S.X. Lv, J.C. Feng, Novel design of tool for joining hollow extrusion by friction stir welding, *Sci. Technol. Weld. Joi.* 18 (2013) 239-246.
- [8] M. Skinner, R.L. Edwards, Improvements to the FSW process using the self-reacting technology, *Mater. Sci. Forum* 426-432 (2003) 2849-2854.
- [9] L. Wan, Y. Huang, Z. Lv, S. Lv, J. Feng, Effect of self-support friction stir welding on microstructure and microhardness of 6082-T6 aluminum alloy joint, *Mater. Des.* 55 (2014) 197-203.
- [10] H.J. Liu, J.C. Hou, H. Guo, Effect of welding speed on microstructure and mechanical properties of self-reacting friction stir welded 6061-T6 aluminum alloy, *Mater. Des.* 50 (2013) 872-878.
- [11] K. Okamoto, A. Sato, S.H.C. Park, S. Hirano, Microstructure and mechanical properties of FSWed aluminum extrusion with bobbin tools, *Mater. Sci. Forum* 706-709 (2012) 990-995.
- [12] M.K. Sued, D. Pons, J. Lavroff, E.H. Wong, Design features for bobbin friction stir welding tools: Development of a conceptual model linking the underlying physics to the production process, *Mater. Des.* 54 (2014) 632-643.
- [13] J.A. Schneider, A.C. Nunes, M.S. Brendel, The influence of friction stir weld tool form and welding parameters on weld structure and properties: nugget bulge in self-reacting friction stir welds, In: 8th International Symposium on Friction Stir Welding, May 18-20, Timmendorfer Strand (Germany), 2010.
- [14] ASTM E8/E8M-13a. Standard test methods for tension testing of metallic materials, West Conshohocken, PA: ASTM International; 2013.
- [15] R.D. Fu, J.F. Zhang, Y.J. Li, J. Kang, H.J. Liu, F.C. Zhang, Effect of welding heat input and post-welding natural aging on hardness of stir zone for friction stir-welded 2024-T3 aluminum alloy thin-sheet, *Mater. Sci. Eng. A* 559 (2013) 319-324.

- [16] J. Shen, F. Wang, U.F.H. Suhuddin, S. Hu, W. Li, J.F. dos Santos, Crystallographic texture in bobbin tool friction-stir welded aluminum, *Metall. Mater. Trans. A* 46 (2015) 2809-2813.
- [17] Y. Zhao, Q. Wang, H. Chen, K. Yan, Microstructure and mechanical properties of spray formed 7055 aluminum alloy by underwater friction stir welding, *Mater. Des.* 56 (2014) 725-730.
- [18] Y.S. Sato, F. Yamashita, Y. Sugiura, S.H.C. Park, H. Kokawa, FIB-assisted TEM study of an oxide array in the root of a friction stir welded aluminium alloy, *Scripta Mater.* 50 (2004) 365-369.
- [19] Y.S. Sato, H. Takauchi, S.H.C. Park, H. Kokawa, Characteristics of the kissing-bond in friction stir welded Al alloy 1050, *Mater. Sci. Eng. A* 405 (2005) 333-338.
- [20] H.J. Liu, Y.C. Chen, J.C. Feng, Effect of zigzag line on the mechanical properties of friction stir welded joints of an Al-Cu alloy, *Scripta Mater.* 55 (2006) 231-234.
- [21] Z. Zhang, B.L. Xiao, Z.Y. Ma, Effect of segregation of secondary phase particles and “S” line on tensile fracture behavior of friction stir-welded 2024Al-T351 joints, *Metall. Mater. Trans. A* 44 (2013) 4081-4097.
- [22] T.L. Jolu, T.F. Morgeneyer, A.F. Gourgues-Lorenzon, Effect of joint line remnant on fatigue lifetime of friction stir welded Al-Cu-Li alloy, *Sci. Technol. Weld. Joi.* 15 (2010) 694-698.
- [23] C.B. Fuller, M.W. Mahoney, M. Calabrese, L. Micona, Evolution of microstructure and mechanical properties in naturally aged 7050 and 7075 Al friction stir welds, *Mater. Sci. Eng. A* 527 (2010) 2233-2240.
- [24] J.Q. Su, T.W. Nelson, R. Mishra, M. Mahoney, Microstructural investigation of friction stir welded 7050-T651 aluminium, *Acta Mater.* 51 (2003) 713-729.
- [25] S.A. Khodir, T. Shibayanagi, M. Naka, Microstructure and mechanical properties of friction stir welded AA2024-T3 aluminum alloy, *Mater. Trans.* 47 (2006) 185-193.
- [26] M.N. Ilman, Kusmono, P.T. Iswanto, Fatigue crack growth rate behaviour of friction-stir aluminium alloy AA2024-T3 welds under transient thermal tensioning, *Mater. Des.* 50 (2013) 235-243.
- [27] A.K. Shukla, W.A. Baeslack, Study of process/structure/property relationships in friction stir welded thin sheet Al-Cu-Li alloy, *Sci. Technol. Weld. Joi.* 14 (2009) 376-387.

- [28] A. Steuwer, M. Dumont, J. Altenkirch, S. Biroscia, A. Deschamps, P.B. Prangnell, P.J. Withers, A combined approach to microstructure mapping of an Al-Li AA2199 friction stir weld, *Acta Mater.* 59 (2011) 3002-3011.
- [29] T.L. Jolu, T.F. Morgeneyer, A. Denquin, M. Sennour, A. Laurent, J. Besson, A. Françoise, G. Lorenzon, Microstructural characterization of internal welding defects and their effect on the tensile behavior of FSW joints of AA2198 Al-Cu-Li alloy, *Metall. Mater. Trans. A* 45 (2014) 5531-5544.
- [30] W. Li, R. Jiang, Z. Zhang, Y.E. Ma, Effect of rotation speed to welding speed ratio on microstructure and mechanical behavior of friction stir welded aluminum-lithium alloy joints, *Adv. Eng. Mater.* 15 (2013) 1051-1058.

Table and Figure captions

Table 1 Chemical composition of AA2198 (wt. %) alloy

Table 2 List of welding parameters with the measured variables in this study

Table 3 Grain structure characteristics in different zones

Fig. 1 The welding thermal cycles of the joints produced with different rotational speeds.

Fig. 2 (a) A macrograph showing a typical BT-FSW joint overlaid with the probe profile; EBSD micrographs showing the grain morphologies of (b) the BM; (c) the TMAZ on the AS; (d) the SZ; and (e) the TMAZ on the RS.

Fig. 3 Optical microstructures and grain size of the SZs obtained at different rotational speeds: (a) 400 rpm, $2.1 \pm 0.2 \mu\text{m}$; (b) 600 rpm, $3.9 \pm 0.1 \mu\text{m}$; (c) 800 rpm, $4.8 \pm 0.2 \mu\text{m}$; and (d) 1000 rpm, $6.0 \pm 0.3 \mu\text{m}$.

Fig. 4 (a) negative optical macrographs of joints produced at different rotational speeds, after being etched by a 2% NaOH solution; (b) a backscattered electron micrograph showing the detail of the JLR region, without etching; (c) a schematic diagram showing the influence of the rotational speed on the position and morphology of the JLR.

Fig. 5 (a) hardness along the mid-thickness of the joints at different rotational speeds; (b) schematic of W-shaped and U-shaped hardness profiles; and (c) 2D hardness maps through the joints superposed with the border of TMAZ/SZ (thick solid black lines) and HAZ/TMAZ (dotted black lines). The dashed black lines and dash-dot white lines denote the position of the edge of the shoulder and of the probe, respectively.

Fig. 6 The influence of the rotational speed on the tensile strength of the joints and result of BM has been included for comparison purposes.

Fig. 7 Typical fracture locations of joints at different rotational speeds: (a) 400 rpm; (b) 600 rpm; (c-d) 800 rpm; and (e-f) 1000 rpm.

Fig. 8 Typical fracture surfaces from different fracture modes: (a) Mode I; (b) Mode II; (c) Mode III; and (d) from the BM.

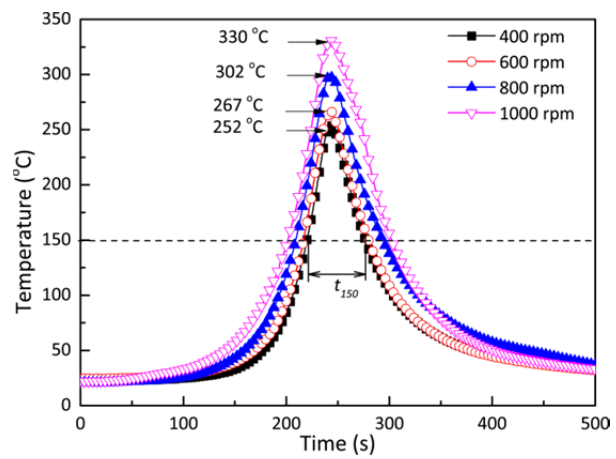


Fig. 1 The welding thermal cycles of the joints produced with different rotational speeds.

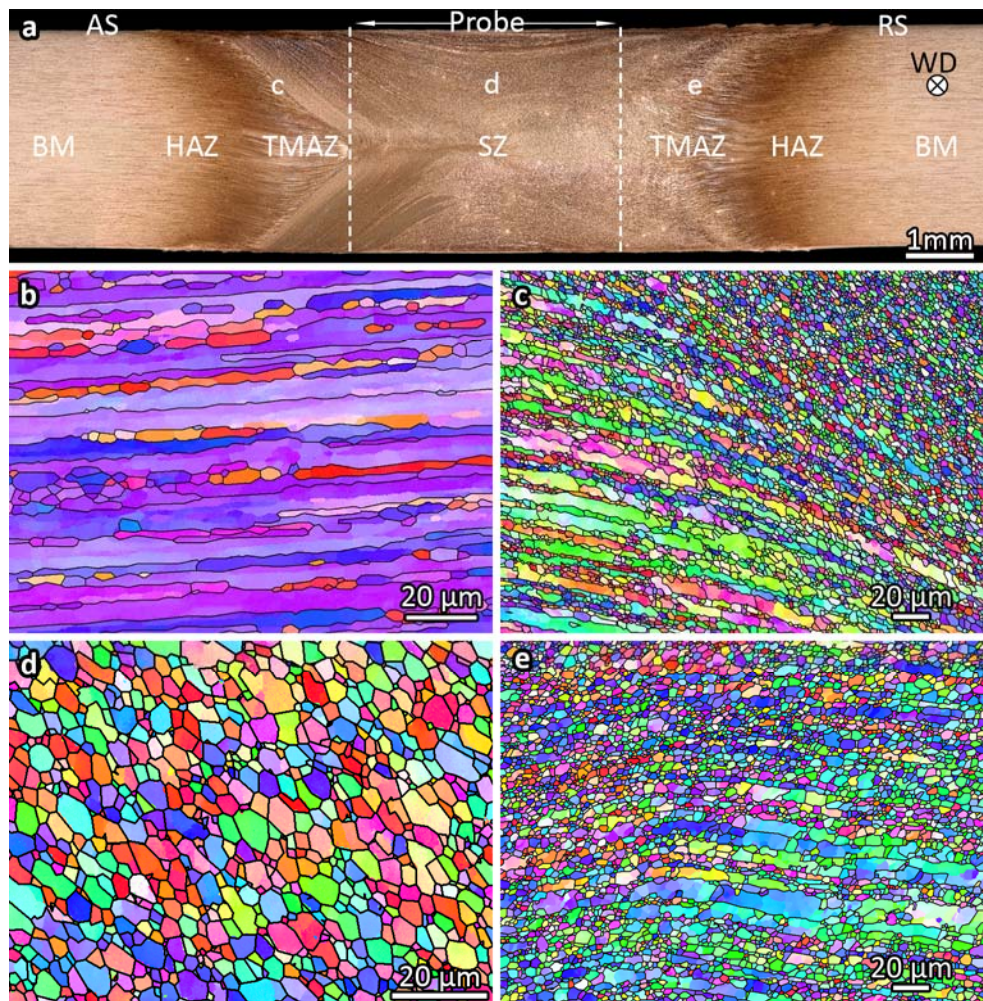


Fig. 2 (a) A macrograph showing a typical BT-FSW joint overlaid with the probe profile; EBSD micrographs showing the grain morphologies of (b) the BM; (c) the TMAZ on the AS; (d) the SZ; and (e) the TMAZ on the RS.

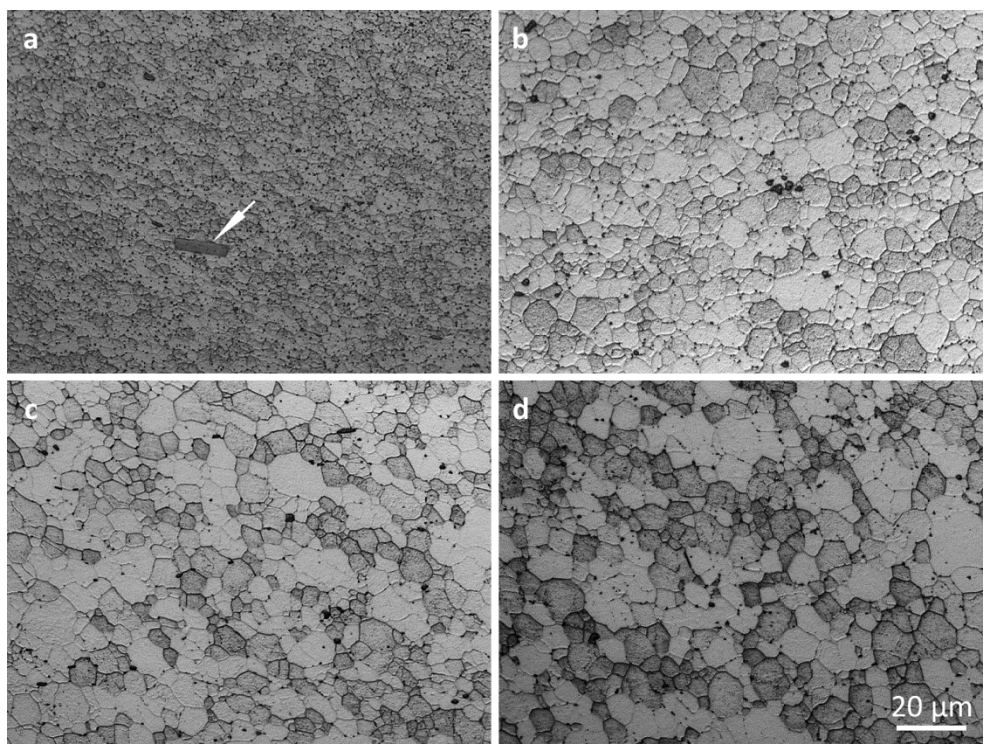


Fig. 3 Optical microstructures and grain size of the SZs obtained at different rotational speeds: (a) 400 rpm, 2.1 ± 0.2 μm ; (b) 600 rpm, 3.9 ± 0.1 μm ; (c) 800 rpm, 4.8 ± 0.2 μm ; and (d) 1000 rpm, 6.0 ± 0.3 μm .

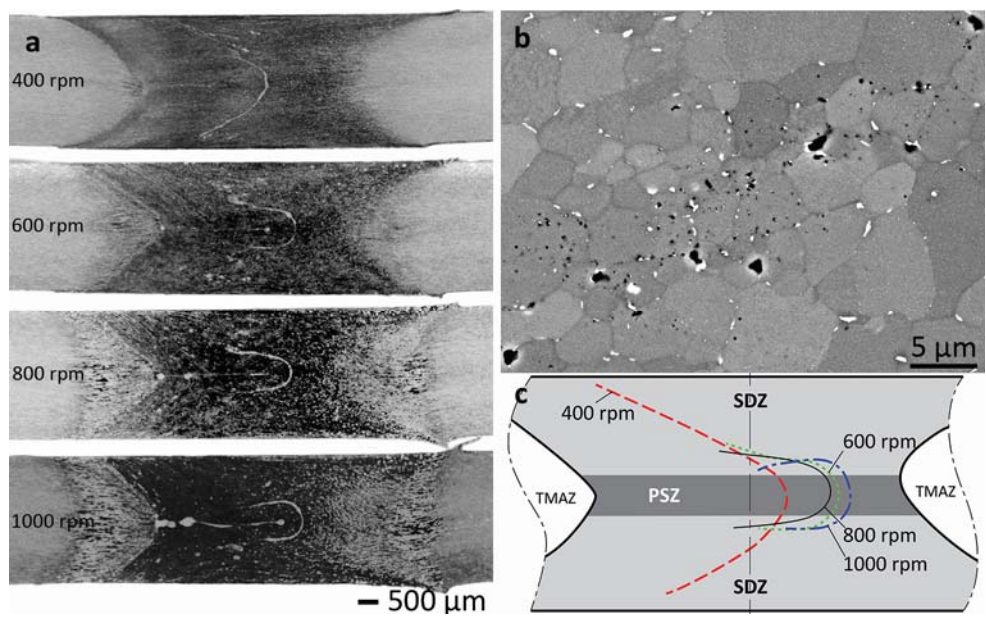


Fig. 4 (a) Negative optical macrographs of joints produced at different rotational speeds, after being etched by a 2% NaOH solution; (b) a backscattered electron micrograph showing the detail of the JLR region, without etching; (c) a schematic diagram showing the influence of the rotational speed on the position and morphology of the JLR.

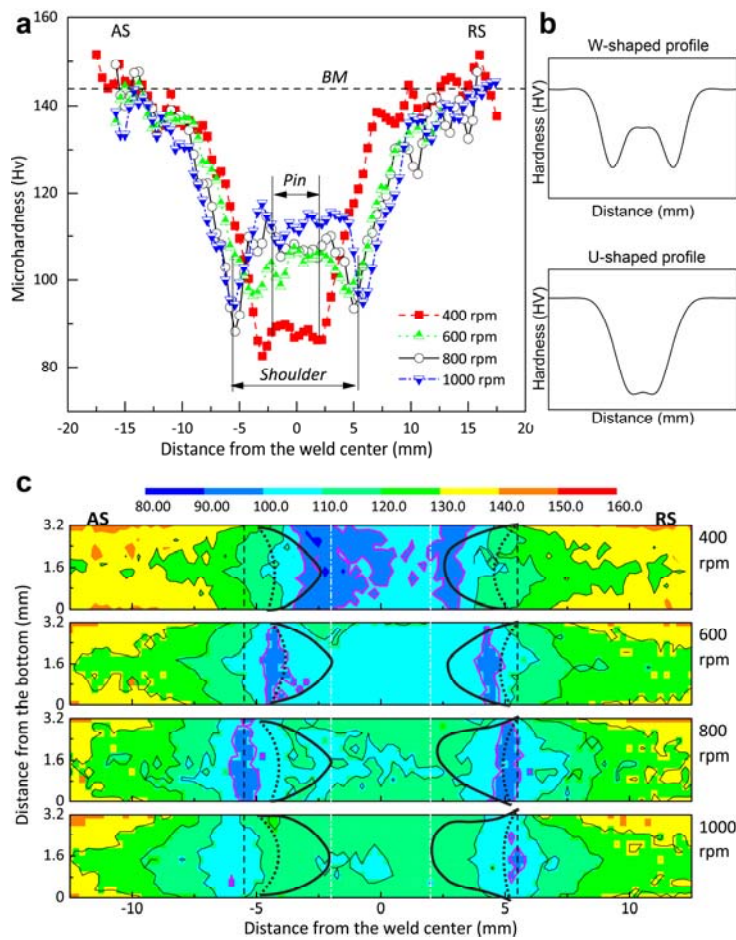


Fig. 5 (a) hardness along the mid-thickness of the joints at different rotational speeds; (b) schematic of W-shaped and U-shaped hardness profiles; and (c) 2D hardness maps through the joints superposed with the border of TMAZ/SZ (thick solid black lines) and HAZ/TMAZ (dotted black lines). The dashed black lines and dash-dot lines denote the position of the edge of the shoulder and of the probe, respectively.

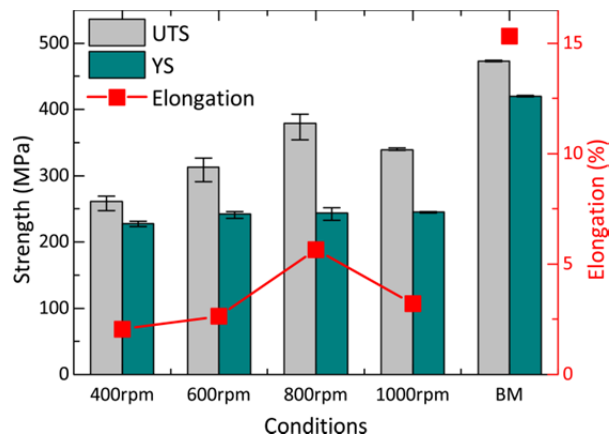


Fig. 6 The influence of the rotational speed on the tensile strength of the joints and result of BM has been included for comparison purposes.

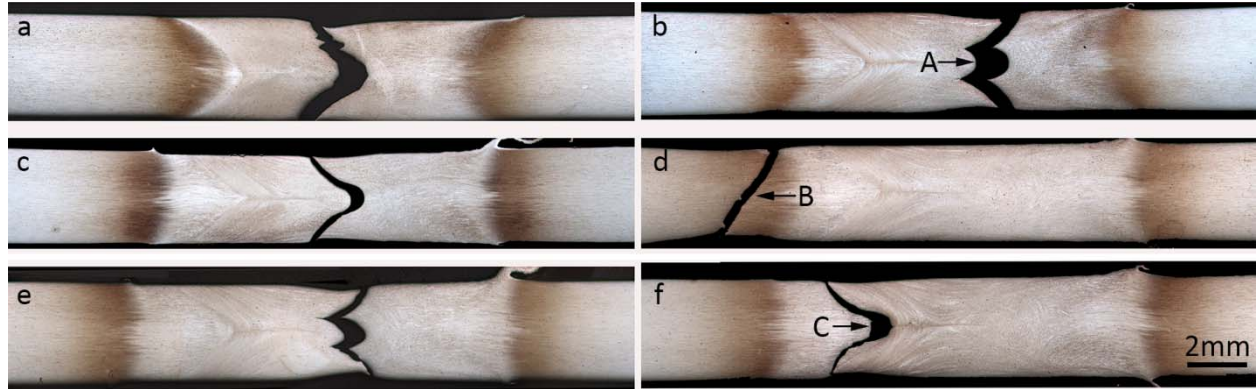


Fig. 7 Typical fracture locations of joints at different rotational speeds: (a) 400 rpm; (b) 600 rpm; (c-d) 800 rpm; and (e-f) 1000 rpm.

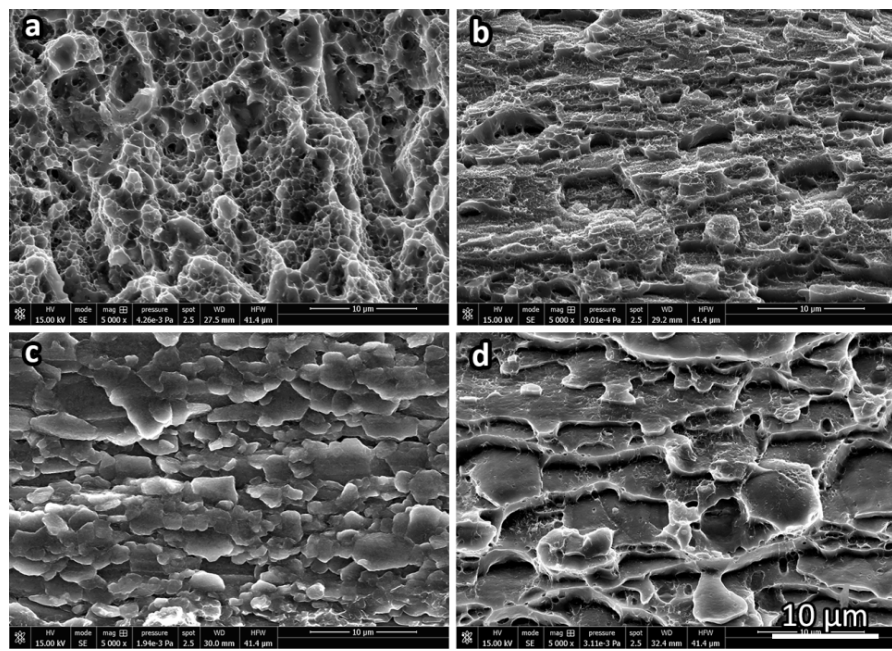


Fig. 8 Typical fracture surfaces from different fracture modes: (a) Mode I; (b) Mode II; (c) Mode III; and (d) from the BM.

Table 1 Chemical composition of AA2198 (wt. %)

| Cu | Li | Mg | Ag | Mn | Zn | Fe | Si | Zr | Al |
|-----|-----|------|------|-------|-------|-------|------|-------|---------|
| 3.2 | 1.0 | 0.31 | 0.27 | 0.005 | 0.014 | 0.046 | 0.03 | 0.076 | Balance |

Table 2 List of welding parameters with the measured variables in this study

| Samples | Rotational speed (rpm) | Welding speed (mm/min) | Gap force (N) | Torque (N·m) | Heat index (J/mm) | Exposure time t_{150} (s) |
|---------|------------------------|------------------------|---------------|--------------|-------------------|-----------------------------|
| BT-11 | 400 | 42 | 1650 | 13.34 | 797.85 | 57 |
| BT-22 | 600 | 42 | 1500 | 10.75 | 964.42 | 64 |
| BT-33 | 800 | 42 | 1350 | 9.00 | 1076.57 | 84 |
| BT-44 | 1000 | 42 | 1150 | 8.35 | 1248.53 | 100 |

Table 3 Grain structure characteristics in different zones

| Zone | High-angle boundary fraction (%) | Average grain size* (μm) | |
|------|----------------------------------|---------------------------------------|------|
| | | OM | EBSD |
| BM | 33.3-35.8 | 2.2 ± 0.2 | 3.0 |
| HAZ | 31.3-32.9 | 2.4 ± 0.3 | 3.1 |
| TMAZ | 52.8-53.2 | - | 4.1 |
| SZ | 36.3 | 3.9 ± 0.1 | 2.7 |

* it is the vertical intercept length for BM and HAZ, while grain diameter for the rest zones